The Stability of Limit-Cycle Oscillations in a Nonlinear Aeroelastic System

S. T. Trickey; L. N. Virgin; E. H. Dowell

Stable URL:

Proceedings: Mathematical, Physical and Engineering Sciences is currently published by The Royal Society.

**THE ROYAL
SOCIETY**

The stability of limit-cycle oscillations in a nonlinear aeroelastic system

BY S. T. TRICKEY, L. N. VIRGIN AND E. H. DOWELL

Pratt School of Engineering, Duke University, Durham, NC 27708-0300, USA

The effects of a freeplay structural nonlinearity on an aeroelastic system are studied experimentally. Particular attention is paid to the stability of a periodic nonlinear aeroelastic response, known as limit-cycle oscillations (LCOs). The major thrust of this research lies in the application of relatively recently developed techniques from nonlinear dynamics and signal processing to the realm of experimental aeroelasticity. Innovations from the field of nonlinear dynamics include time-delay embedded coordinates to reconstruct system dynamics, a Poincaré section to assess the periodic nature of a response and to prescribe an operating point about which a linear description of the dynamics can be approximated, stochastic perturbations to assess the stability and robustness of responses, and a basin of attraction measure to assess initial condition dependence. A novel system-identification approach is used to generate a linear approximation of the experimental system dynamics about the LCO. This technique makes use of a rotating slotted cylinder gust generator and incorporates a least-squares fit of the resulting transient dynamics. An extension to this method is then developed based on the outcome of relatively large disturbances to the flow and hence airfoil, to obtain global stability.

1. Background

Understanding the interaction of fluids and structures has been of interest since even before the invention of heavier-than-air flight vehicles. Theoretical aeroelasticity covers a range of complexity, from simple low-dimensional models to very high-dimensional computational fluid-dynamic (CFD) models. More recent studies in aeroelasticity have begun to focus attention on the effect of nonlinearity on dynamic behaviour. Limit-cycle oscillations (LCOs) are an inherently nonlinear phenomenon and have been observed in a number of experimental (wind-tunnel testing and flight) situations. Thus LCO characterization and explanation is an important goal, not least from the perspective of fatigue and maintenance issues. Nonlinear responses like LCOs have garnered attention due to the intriguing duality they bring to the stability problem. It is sometimes the case that a nonlinearity has the effect of initiating instability, but it also possible for a nonlinear effect to limit the response in an otherwise dangerous situation. Recent articles in *Aviation Week and Space*

Proc. R. Soc. Lond. A (2002) **458**, 2203–2226

2203

Technology have focused on this situation in regard to excessive LCO in the Airbus Industries A319, A320 and A321, and older versions of the Boeing 737.†

Many problems in aeroelasticity are inherently nonlinear and not well described by linear analyses. Fortunately, recent advances in the understanding of nonlinear dynamical systems allows a thorough experimental–theoretical correlation study to be achieved within a fully nonlinear context. When formulating an aeroelastic problem, it is important to establish which aspects of the system require the most accurate representation and what constitutes acceptable approximation error. With the focus on the *structural* nonlinearity of a thin two-dimensional airfoil operating in a low-speed environment, a relatively simple linear theoretical aerodynamic model is justified (Dowell *et al.* 1995).

The primary concern in much of the previous research has been establishing how a particular structural nonlinearity affects the dynamic stability of an aeroelastic system under changing conditions. In the linear model, the dynamics can be categorized based on the system's response to small perturbations. Classic eigenvalue analysis leads directly to the determination of the flutter boundary, i.e. the flow rate at which the response starts to grow without bound (the familiar Hopf bifurcation). An important design (flight-envelope) criterion for an aircraft is the location of this divergent solution or flutter boundary at different operating conditions of the aircraft. The nonlinear model, in addition, can exhibit bounded time-dependent responses including periodic, quasi-periodic and chaotic LCOs. It is the (local and global) stability of these LCOs that is considered, primarily from an experimental perspective, in this paper.

(a) Brief literature survey

A survey of different types of nonlinearity and their effect on aeroelastic behaviour can be found in Breitbach (1977), Dowell *et al.* (1995), Lee *et al.* (1997) and Trickey (2000).

Nonlinear studies in aeroelasticity related to the current work go back to Woolston *et al.* (1955, 1957) and Shen & Hsu (1958). More recently, Price *et al.* (1995) used direct simulation and describing function analysis to study LCOs well below the linear divergent flutter condition, and new results including chaos were presented. A summary of nonlinear techniques can be found in Lee *et al.* (1999a), and application to more specific examples in Raghothama & Narayanan (1999) and Yang & Zhao (1992).

Some experimental results can be found in the work of McIntosh *et al.* (1981) and O'Neil & Stragnac (1998). In both cases, the primary results were a documentation of different types of dynamic behaviour, including LCOs and divergent flutter.

A freeplay-type nonlinearity has been considered in several forms. Lee & Tron (1989) and Price *et al.* (1994) presented results that again demonstrated the existence of LCOs, both periodic and chaotic in nature. Virgin *et al.* (1999) explored the complex dynamic motion possible in the three-degree-of-freedom airfoil model with control surface freeplay and Theodorsen theory aerodynamics. Transitions were observed from stable equilibrium to a periodic LCO to a quasi-periodic

† See, for example, the article 'Airbus elevator flutter: annoying or dangerous' in the 27 August 2001 issue.

Figure 1. Schematic of typical section airfoil model (NACA 0012) with freeplay nonlinearity (δ). Definitions of variables and constants can be found in table 1.

response and finally, via a torus breakdown route, to chaos. Alighanbari & Price (1996) conducted a stability analysis using the AUTO bifurcation analysis software package.

Conner (1996) and Conner *et al.* (1997) use the state-space model proposed by Edwards *et al.* (1979) for a three-degree-of-freedom airfoil with a freeplay in the flap, and reported the important result that all responses scale with freeplay size. Conner *et al.* (1997) also reported on experimental work on a very similar system to the present case, in which a number of LCOs were identified based on a relatively crude root-mean-square measure of the system response. The current paper significantly extends this work by using the latest techniques of nonlinear dynamical systems theory. The theoretical aspects of this work were also complemented by Tang *et al.* (1998), who undertook a parametric study using a describing function (harmonic balance) method to determine the minimum perturbation size necessary to instigate LCO and incorporating an alternative aerodynamic model from Peters & Cao (1995). The concept of using perturbations to investigate the stability of periodic behaviour in experimental mechanical systems was developed in Murphy *et al.* (1994).

The current paper presents both local and global stability results based on both experimental and numerical studies of an airfoil with a freeplay nonlinearity.

2. The aeroelastic system

(a) The mathematical model

The system considered here is a typical section airfoil model (NACA 0012 profile), with control surface freeplay nonlinearity (figure 1). In the theoretical portion of this work, the aerodynamic loads are modelled using an augmented states approximation of Theodorsen theory aerodynamics. Since Theodorsen theory is a standard approach used in low-speed aerodynamics, only a brief summary will be given here. The structural model is developed using Lagrange's equations. A compact matrix form of the equations of motion, presented below, is useful in identifying the major

Table 1. *Definitions of non-dimensional parameters (per unit span)*

m_{ref}	reference mass (wing and flap) (kg m^{-1})	1.716
m_{sup}	support mass (per unit span) (kg m^{-1})	1.814
r_α^2	$I_\alpha/m_{\mathrm{ref}}b^2$	6.840×10^{-1}
r_β^2	$I_\beta/m_{\mathrm{ref}}b^2$	7.336×10^{-2}
x_α	$S_\alpha/m_{\mathrm{ref}}b = m_{\mathrm{ref}}x_{\mathrm{CG}}/m_{\mathrm{ref}}b$	3.294×10^{-2}
x_β	$S_\beta/m_{\mathrm{ref}}b = m_{\mathrm{flap}}x_{\mathrm{CG\,flap}}/m_{\mathrm{ref}}b$	1.795×10^{-2}
K_α	$I_\alpha/m_{\mathrm{ref}}b^2$ (N m kg^{-1} m^{-2})	1.114×10^3
K_β	$I_\beta/m_{\mathrm{ref}}b^2$ (N m kg^{-1} m^{-2})	7.307×10^1
K_h	$S_\alpha/m_{\mathrm{ref}}b = m_{\mathrm{ref}}x_{\mathrm{CG}}/m_{\mathrm{ref}}b$ (N kg^{-1})	1.724×10^3
ζ_α	pitch modal damping ratio	1.0×10^{-2}
ζ_β	flap modal damping ratio	1.2×10^{-2}
ζ_h	plunge modal damping ratio	1.5×10^{-2}
$\omega_\alpha/2\pi$	pitch-coupled natural frequency (Hz)	8.308
$\omega_\beta/2\pi$	flap-coupled natural frequency (Hz)	2.1403
$\omega_h/2\pi$	plunge-coupled natural frequency (Hz)	4.475
κ	$\pi\rho b^2/m_{\mathrm{ref}}$ = mass ratio	3.646×10^{-2}

contributing elements to the dynamics;

$$\left(M_{\mathrm{s}} - \frac{\kappa}{\pi}M_{\mathrm{NC}}\right)\ddot{X} + \left(B_{\mathrm{s}} - \frac{\kappa}{\pi}\left(\frac{U}{b}\right)[B_{\mathrm{NC}} + \tfrac{1}{2}RS_2]\right)\dot{X}$$

$$+ \left(K_{\mathrm{s}} - \frac{\kappa}{\pi}\left(\frac{U}{b}\right)^2[K_{\mathrm{NC}} + \tfrac{1}{2}RS_1]\right)X$$

$$= \frac{\kappa}{\pi}\left(\frac{U}{b}\right)\left(R\left[C_2C_4(C_1+C_3)\left(\frac{U}{b}\right)^2(C_1C_2+C_3C_4)\left(\frac{U}{b}\right)\right]\right)X_{\mathrm{aug}}. \quad (2.1)$$

Here, the system state vector is $X = [\alpha\beta h]^{\mathrm{T}}$, which is comprised of the pitch, flap and plunge coordinates. The augmented state vector, $X_{\mathrm{aug}} = [x\dot{x}]^{\mathrm{T}}$, contains the aerodynamic states that are related to the dynamics of the physical portion of the system through the following ordinary differential equation (ODE),

$$\ddot{x} = \left[-C_2C_4\left(\frac{U^2}{b}\right) \quad -(C_2+C_4)\left(\frac{U}{b}\right)\right]X_{\mathrm{aug}} + \left[\left(\frac{U}{b}\right)S_1\right]X + [S_2]\dot{X}, \quad (2.2)$$

a time-domain transformation of the frequency-domain approximation of the Wagner indicial lift function.

In (2.1), the M_{s}, B_{s} and K_{s} matrices describe the physical characteristics of the airfoil, namely the mass, damping and stiffness. The mass matrix is full, indicating inertial or dynamic coupling. The damping matrix is constructed assuming a modal damping model and the stiffness matrix is diagonal. We note that the stiffness matrix contains the only nonlinearity present in the system. The exact form of these matrices and the matrices describing the aerodynamic properties of the system can be found in Edwards *et al.* (1979), Lee *et al.* (1999*b*) and Trickey (2000). The specific non-dimensional values necessary to construct the matrices can be found in table 1.

The non-circulatory aerodynamic matrices, M_{NC}, B_{NC} and K_{NS}, account for the presence of the airfoil in the airstream. The remaining terms (the vectors R, S_1, S_2,

the constants C_i and the augmented state vector X_{aug}) constitute the effects of the wake dynamics on the airfoil according to an approximation of Theodorsen theory aerodynamics. It should be noted that, with the exception of the M_{NC} term, all of the aerodynamic modelling components include a dependence on the flow speed, U.

The nonlinearity in the system, alluded to earlier, appears in the 2, 2 term of the structural stiffness matrix, K_s. The flap-restoring torque (see inset of figure 1) takes the form

$$\tau_\beta = \begin{cases} 0, & |\beta| \leqslant \delta, \\ K_\beta(\beta - \delta), & |\beta| > \delta. \end{cases} \tag{2.3}$$

The nonlinear consequence of this form of restoring torque is that the stiffness matrix depends on the system state. In addition, the constant offset term, $K_\beta\delta$, is required to model the dynamics correctly when the system leaves the flap stiffness dead-band.

The numerical integrations carried out in the simulations conducted in this work were performed using an adaptive time-step Runge–Kutta algorithm with the fourth/fifth-order formulation from *Numerical recipes in C* (Press *et al.* 1992). Additional simulations were carried out with the MATLAB software package. Numerical integration usually requires equations of motion to be cast into a set of first-order coupled ODEs. Casting the combination of (2.1) and (2.2) into first-order form gives

$$\dot{Y} = A_i Y + b_i, \quad i = 0, 1, \tag{2.4}$$

where $Y = [\alpha \ \beta \ h \ \dot{\alpha} \ \dot{\beta} \ \dot{h} \ x \ \dot{x}]^T$ and A_i and b_i have the block forms

$$A_i = \begin{bmatrix} 0 & I & 0 \\ -M_T^{-1}K_T & -M_T^{-1}B_T & M_T^{-1}D \\ \begin{bmatrix} 0 \\ \tilde{S}_1 \end{bmatrix} & \begin{bmatrix} 0 \\ S_2 \end{bmatrix} & F \end{bmatrix}, \quad b_0 = \{0\}, \quad b_1 = \left\{ \begin{matrix} 0 \\ M_T^{-1} \begin{Bmatrix} 0 \\ K_\beta\delta \\ 0 \end{Bmatrix} \\ 0 \end{matrix} \right\}, \tag{2.5}$$

where the subscript 'T' stands for total. K_T in matrix A_0 uses the structural stiffness matrix K_s with zero flap stiffness, while the A_1 matrix includes the nominal linear flap stiffness in the K_s matrix.

One further modelling point to make is the care that is required in switching between the $i = 0$ (within deadband) and $i = 1$ (outside deadband) sets of equations. Since the eigenvalues of A_0 are similar in magnitude to those of A_1, the Runge–Kutta algorithm performs well. A system with a very stiff K_β would degrade the performance of the Runge–Kutta solver and would have to be replaced by a stiff ODE solver. The actual mechanics of switching sets of equations on the edge of the deadband region is accomplished using the method described by Henon (1982) and commonly known as the technique of inverse interpolation. In order to arrive at the exact transition point from one set of equations to another, which is simply when $|\beta| = \delta$, the method of inverse interpolation involves exchanging the independent variable time with the dependent variable β. After making this switch, it is a simple matter to integrate until $|\beta| = \delta$. Additional discussion of this method can be found in Conner (1996).
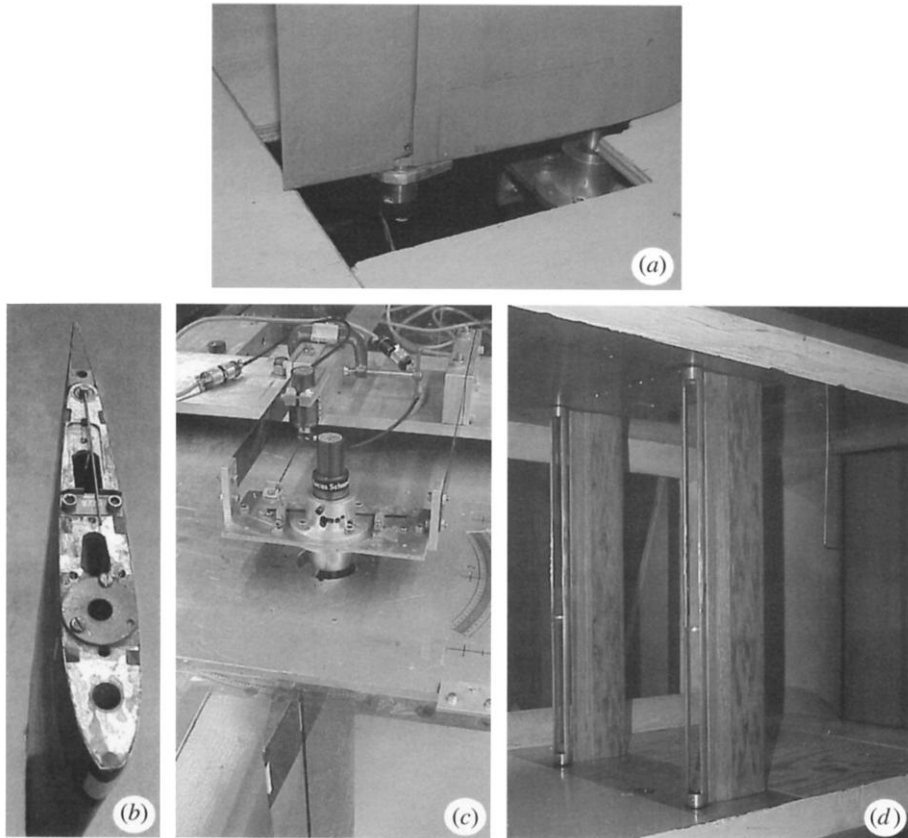
Figure 2. Details of the experimental model. (*a*) Flap RVDT transducer. (*b*) Flap stiffness assembly. (*c*) Pitch and plunge stiffness assemblies with RVDT transducers. (*d*) The gust-generator assembly.

(*b*) *The experimental model*

The physical model used in all of the wind-tunnel tests (figure 2) is described in Conner (1996). The wing section has a span of 0.52 m, which, when installed in the $0.55 \times 0.65 \times 1.55$ m^3 test section of the wind tunnel, is intended to represent the analytical model presented earlier. The additional dimensional parameters that completely describe the model can be found in Conner (1996). See table 1 for the set of the non-dimensional parameters based on the experimental model. The short cantilevered rod-and-bracket assembly (figure 2*a*) gives the model the desired piecewise linear flap-restoring torque. A set of matching leaf springs gives the model stiffness in the plunge coordinate (figure 2*c*). A similar rod runs through the pitch-mounting axle and gives the model its pitch stiffness.

Three rotary variable differential transformers (RVDTs), one attached to the pitch rotational axis, one attached to the flap rotational axis and one attached via an extension rod from the fixed frame to the moving mounting brackets, provide for measurement of the pitch, flap and plunge displacements. After observing typical signal-to-noise ratios of $\text{SNR}_\alpha = 48$, $\text{SNR}_\beta = 136$ and $\text{SNR}_h = 16$ for a typical flap-buzzing-type oscillatory response, the decision was made to rely on the flap

transducer and the embedding concept of nonlinear dynamic theory to record the dynamics of the system. A typical plunge-dominated motion also resulted in the highest signal-to-noise ratio in the β state variable. Here, SNR is defined as

$$\mathrm{SNR}_i = 20\log\frac{\sigma_i}{\sigma_{Ni}}, \quad i = \alpha, \beta, h, \tag{2.6}$$

where σ_i is the standard deviation of the transducer signal during a characteristic oscillation and $\sigma_{N,i}$ is the standard deviation of the transducer signal noise in a static state.

A final note concerning the experimental model is appropriate. The model exhibited a sensitivity to its installation conditions. Across the different installations of this experiment, values of natural frequencies and damping levels, along with the initial angle of attack set during each installation, showed some variability. While this is to be expected in an experimental setting, the implication is that some behaviour can only be qualitatively compared between similar systems as precise system-property measurements were found to be elusive.

The application of the perturbation approach is based on the gust-generator device pictured in figure 2d. The capability of this type of gust generator to disturb the flow field has been investigated numerically (Cizmas *et al.* 1996) and experimentally (Tang *et al.* 1996; Tang & Dowell 1996). This system consists of a pair of slotted cylinders, which can be made to spin at a user-prescribed rate and thus disturb in the flow onto the airfoil. While there are three-dimensional aspects of the flow field created by the generator, the gust waveform is primarily planar and thus can be approximated as a two-dimensional perturbation, consistent with the airfoil model used in this study. Also shown forward of the gust generator in figure 2 is a pitot tube, which was used to measure flow speed. Data were acquired using a National Instruments PCI-6024E data-acquisition board in combination with a suite of LabVIEW applications.

3. Limit-cycle oscillations

In this section we examine the limit-cycle response of the airfoil as a function of flow rate. The underlying linear system gives some clues to anticipated behaviour, but in general the responses found are thoroughly nonlinear. Two extremes of the freeplay can be considered. First, if the freeplay exists for all flap amplitudes (thus the flap stiffness is zero), the system undergoes classic linear flutter at a flow speed of approximately $4.48\,\mathrm{m\,s}^{-1}$. This value was obtained from a standard linear eigenvalue analysis (Dowell *et al.* 1995). Second, if the freeplay does not exist for any flap amplitudes (thus giving a nominal linear flap stiffness), the critical flutter boundary is shifted to $22.14\,\mathrm{m\,s}^{-1}$. In both of these cases, the plunge mode initiates the instability. With a limited freeplay range in the flap amplitude, a variety of dynamic responses are possible, and these will be summarized in the next section.

(a) Bifurcation diagrams

Bifurcation diagrams are a diagnostic tool used to characterize complicated changes of a system as a function of a changing parameter. Here, the bifurcation diagram is generated by measuring the value of the flap angle displacement whenever
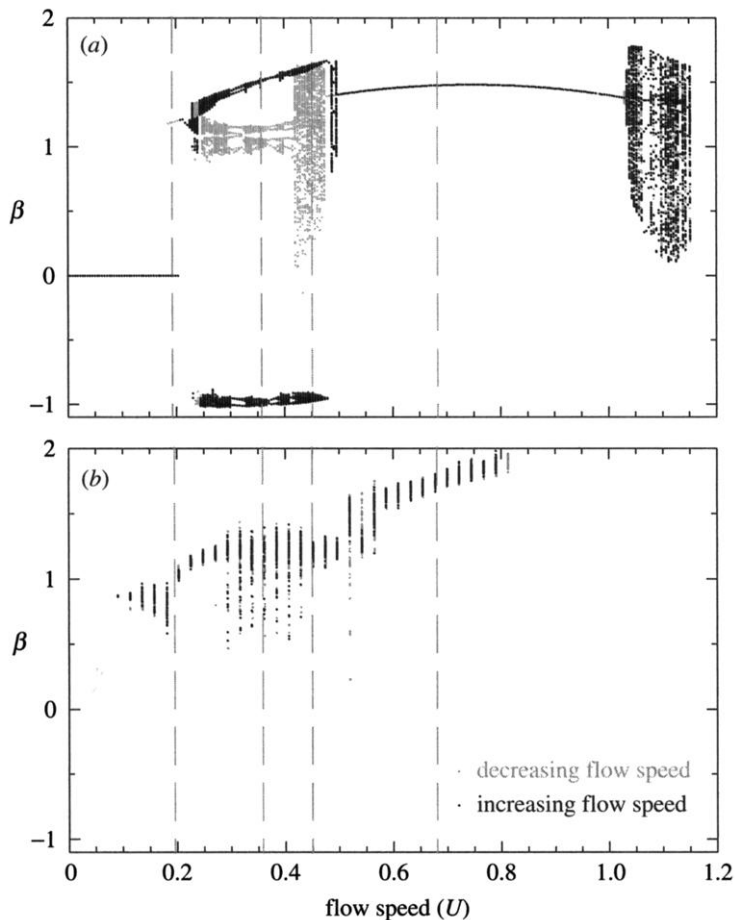
Figure 3. Numerical and experimental bifurcation diagrams.
Decreasing flow indicated by grey dots. Increasing flow indicated by black dots.

the flap velocity passes through zero from above. In this form, a bifurcation diagram would display the magnitude of a simple harmonic response as a single point. The true utility of a bifurcation diagram becomes apparent as responses become more complicated.

Figure 3 contains the bifurcation diagrams of the (a) numerical and (b) experimental system. The flow rate is non-dimensionalized (in both simulation and experiment) with respect to the linear flutter boundary associated with the aforementioned no-freeplay case where $u_{\mathrm{l}} = 22.14\,\mathrm{m\,s^{-1}}$, i.e. $U = u/u_{\mathrm{l}}$. The responses that follow are generally illustrated by the flap displacement, which is non-dimensionalized by the freeplay, i.e. $\beta = 1$ corresponds to initial contact. A number of distinct regions of different types of behaviour can be observed in the simulation results: stationary ($U = 0$–0.2), non-simple LCO ($U = 0.25$–0.27), chaotic ($U \approx 0.45$) and simple LCO ($U > 0.5$). Also in this chaotic range are the quasi-periodic responses discussed in considerably more detail by Conner (1996) and Virgin *et al.* (1999). Both increasing and decreasing flow rates are included in order to establish the hysteretic nature of some of these responses. Clearly, this situation is considerably more complicated
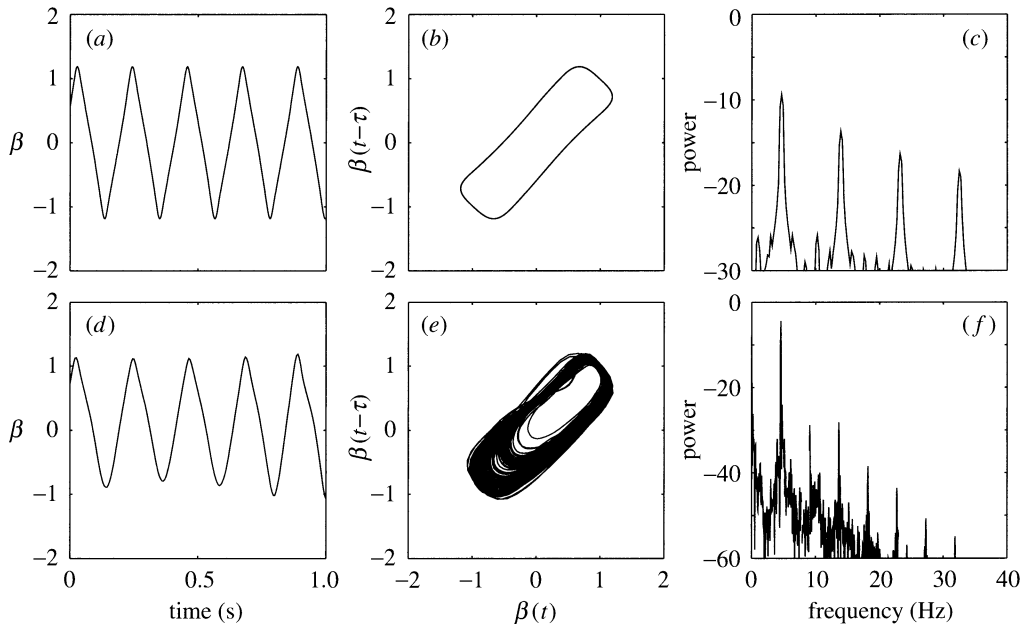
Figure 4. Numerical and experimental snapshots of the system behaviour in terms of (*a*), (*d*) time-series, (*b*), (*e*) phase projection and (*c*), (*f*) power spectrum. (*a*), (*b*), (*c*) Theory. (*d*), (*e*), (*f*) Experiment. $U = 0.192$.

than the underlying linear system response, which consists of stationarity followed by unlimited divergence.

The experimental bifurcation diagram shows little evidence of the hysteresis seen in the numerical version or the experimental spectrograms, which is further indication of the experimental systems variability, although other installations of the airfoil did lead to a greater regime of hysteresis. The clean nature of the numerical bifurcation in figure 3 clearly shows the intricate evolution of the systems behaviour. However, the background flow turbulence in the wind tunnel obscures the finer details of the dynamics of the experimental system.

As an aside, one final observation is warranted with regard to the numerical bifurcation diagram of figure 3. The system undergoes a complex evolution of dynamical behaviour as it approaches divergent flutter. Recall the no-freeplay linear flutter speed is $U = 1.0$ ($u_1 = 22.14 \text{ m s}^{-1}$)—a point very close to the onset of the complicated dynamics. Windows of periodic behaviour appear and disappear in amongst much more complicated non-periodic behaviour. This includes transitions between periodic, quasi-periodic and chaotic behaviour in remarkably generic patterns, such as torus breakdown with frequency locking, that are of the same form as those seen in the much simpler circle map (Ott 1993).

(*b*) *Specific types of response*

Some characteristic responses (their locations indicated by the vertical grey lines in figure 3) are now illustrated using time histories, phase projections and power spectra. Prior to the initial onset of LCO, the airfoil is, of course, stationary. A small amount of hysteresis (and hence initial condition dependence) has been detailed from
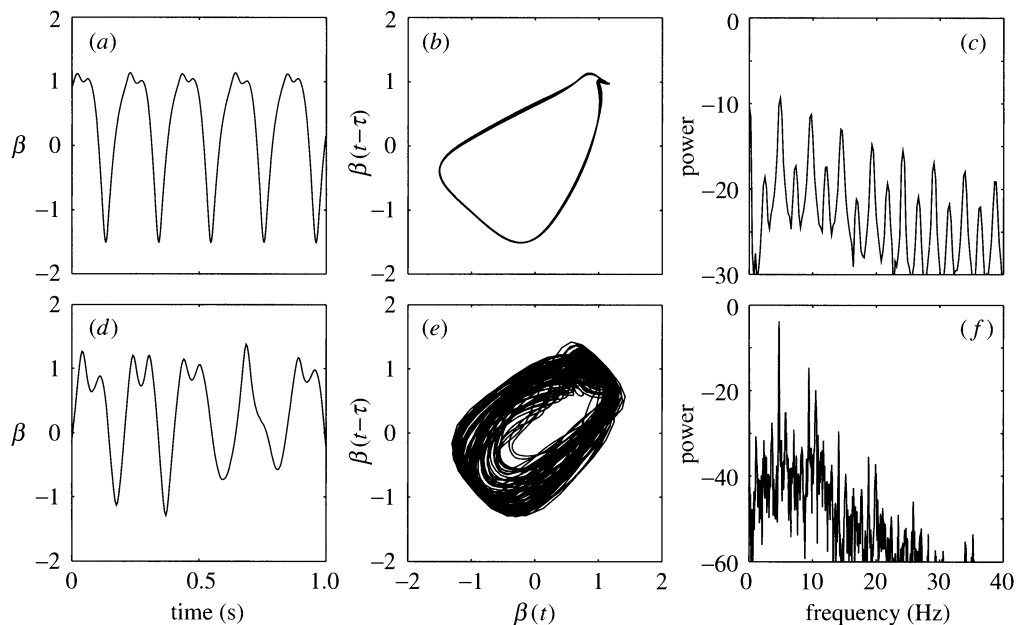
Figure 5. Numerical and experimental snapshots of the system behaviour in terms of (a), (d) time-series, (b), (e) phase projection and (c), (f) power spectrum. (a), (b), (c) Theory. (d), (e), (f) Experiment. $U = 0.361$.

an approximate analytical perspective (Tang *et al.* 1998). Figure 4 shows the low-speed periodic response. The triangle-type waveform seen in the time history explains the presence of odd harmonics in the power spectrum (i.e. ω_0, $3\omega_0$, $5\omega_0$, etc.). The embedded time-phase projection shows the single open loop of a period-one response. The velocity is relatively constant between impacts.

The relatively thick spread apparent in the phase projection is due to the typical wind-tunnel (mildly turbulent) flow conditions, although this effect is not as pronounced at higher flow rates.

Figure 5 shows an asymmetric solution where the flap response extends well into the stiffness on one side of the deadband but only 'taps' the stiff region on the opposite side of the deadband. Once a steady-state response has been achieved, one can switch between this and a mirror-image solution at will by negating the structural components of the state and leaving the augmented states unaltered. This response is characterized by the strong harmonic of the cross deadband motion and the weak harmonic or sub-harmonic of the tap motion. The wind-tunnel turbulence has a more profound effect on the tapping-type response, as might be expected when considering the system response from the perspective of an impact oscillator (Virgin 2000).

Figure 6 displays the broadband response of the system. The experimental version is from a previous installation in the wind tunnel, with a non-zero initial angle of attack, which causes a biased one-sided response. Calculations of a fractional attractor dimension and a positive Lyapunov exponent (both well-established measures from nonlinear dynamic theory (see, for example, Strogatz 1994; Virgin 2000)) indicate that the response should be classified as chaotic, although for some experimental
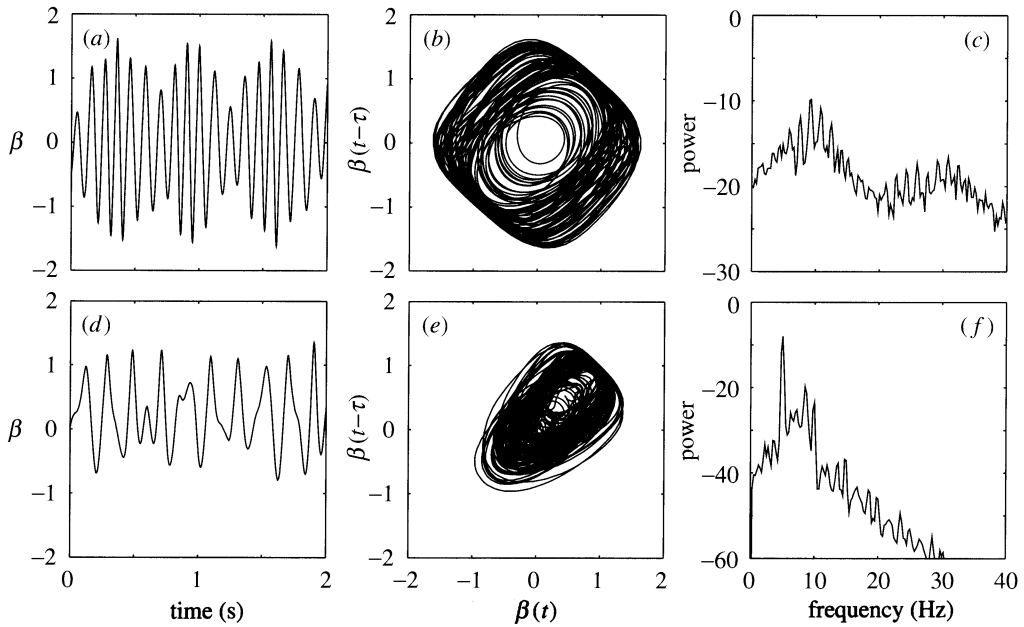
Figure 6. Numerical and experimental snapshots of the system behaviour in terms of (a), (d) time-series, (b), (e) phase projection and (c), (f) power spectrum. (a), (b), (c) Theory. (d), (e), (f) Experiment. $U = 0.452$.

runs it appeared that a quasi-periodic motion anticipated from numerical simulation was also present.

The response shown in figure 7 is a simpler harmonic response, akin to the LCO response seen at a flow velocity of $U = 0.192$, with a fundamental frequency roughly twice as great as that at smaller U. The transition to this kind of 'buzz' response was abrupt. The relatively large 20 Hz harmonic component seen in the experimental results could be attributed to the asymmetry imparted from the small but unavoidable initial angle of attack.

(c) Spectrograms

Figures 8–10 are spectrogram plots generated by recording time histories at set flow speeds, windowing with a Hanning window, then calculating the power spectrum of the signal. Collecting the results over several flow speeds and plotting the contours of the resulting power-spectrum surface displays the frequency content of the responses at different flow speeds. This may be considered as the frequency-domain analogue to the bifurcation diagrams shown earlier. Hysteresis in the response again necessitates two versions of the spectrogram—one with increasing flow speed and another with decreasing flow speeds. After completing static and dynamic 'ground' tests to measure stiffness and damping characteristics of the experimental model, matching the spectrogram response between theory and experiment was found to be particularly helpful in establishing the appropriate parameters for the numerical simulation.

In figure 8, again a number of distinct regions can be seen from the numerical simulation responses, i.e. a low-speed ($U = 0.2$–0.27 in the increasing-flow case)
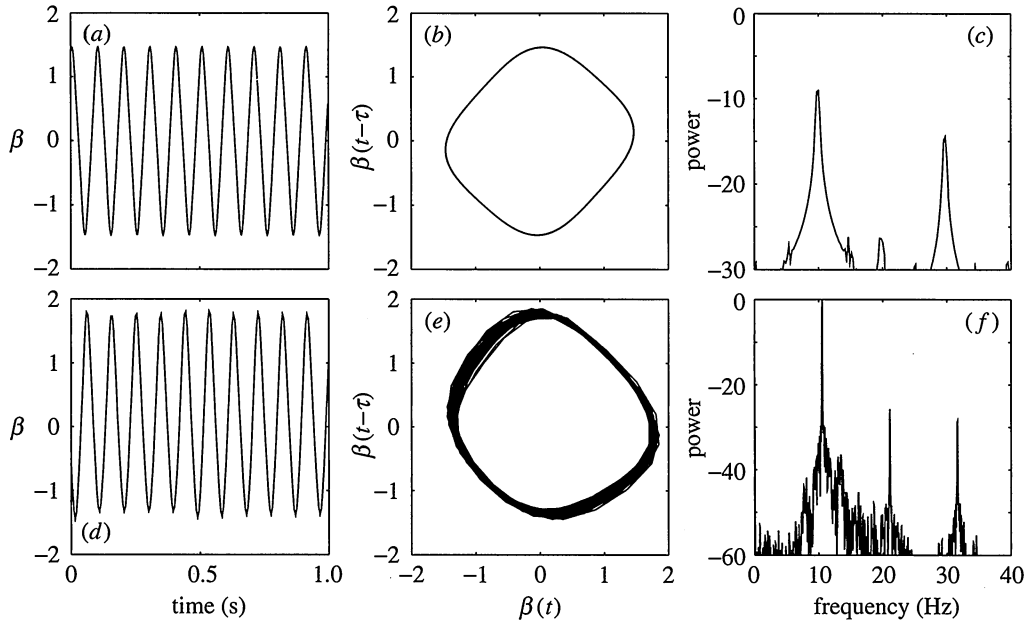
Figure 7. Numerical and experimental snapshots of the system behaviour in terms of (a), (d) time-series, (b), (e) phase projection and (c), (f) power spectrum. (a), (b), (c) Theory. (d), (e), (f) Experiment. $U = 0.678$.
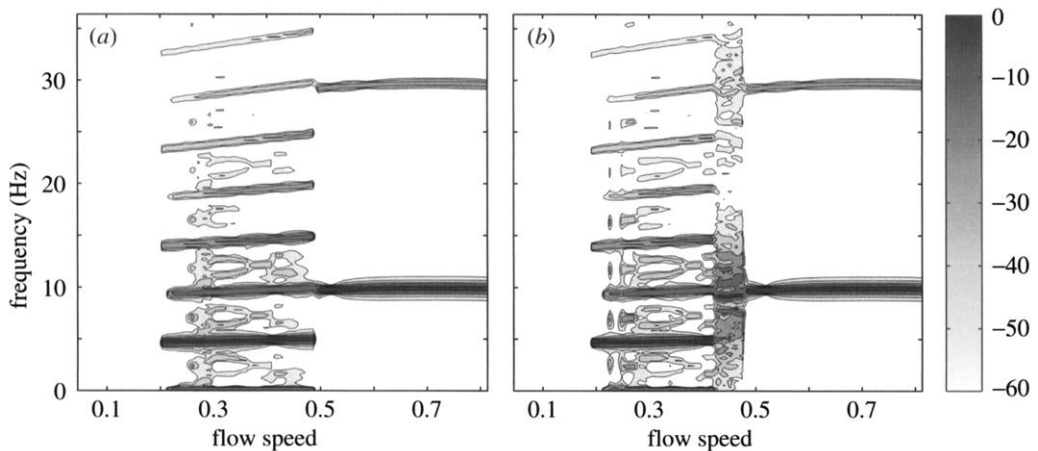

Figure 8. Numerical spectrograms with (a) increasing and (b) decreasing flow speed. The magnitude of the power spectrum is measured in dB.

multi-harmonic response, a medium-flow ($U = 0.27$–0.41) multi-harmonic response with strong and weak harmonics, a broadband response (flow speed approximately $U = 0.45$, with decreasing flow) and a two-frequency simple-periodic response for large flow speeds ($U = 0.5+$).

Figure 9 shows the spectrograms of the experimental system. The results show the low-speed multi-harmonic and high-speed simple-periodic response, although in both cases there is an additional harmonic at *ca.* 20 Hz not captured in the numerical simu-
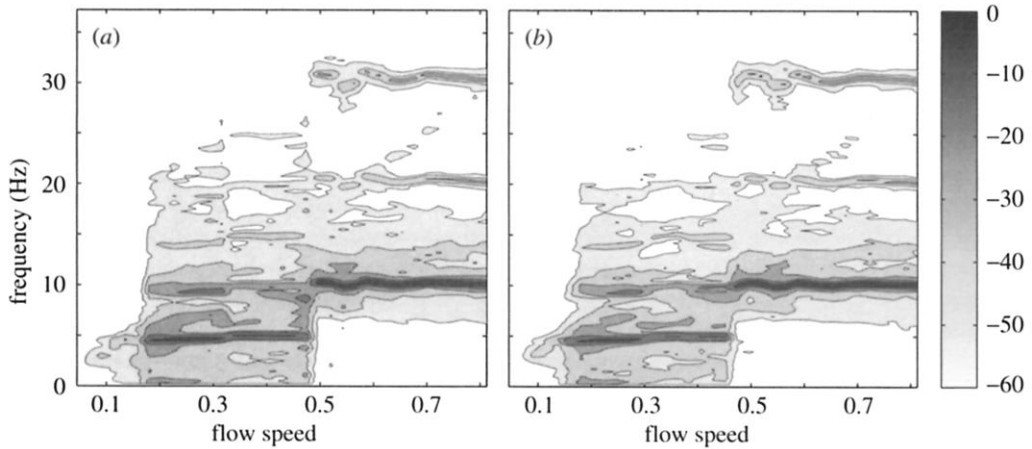
Figure 9. Experimental spectrograms with (*a*) increasing and (*b*) decreasing flow speed. The magnitude of the power spectrum is measured in dB.
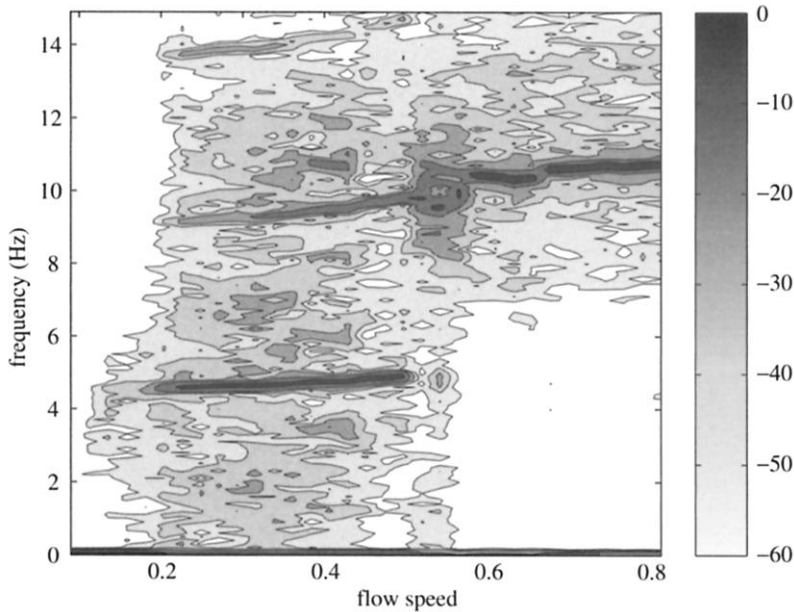

Figure 10. A higher resolution experimental spectrogram with increasing flow speed (and based on a slightly different installation).

lation. The system of figure 9 did not exhibit the broadband response, although other installations of the experimental configuration did (at approximately $U = 0.54$). Although harder to distinguish due to a less-refined frequency grid, figure 9 does show evidence of the strong and weak harmonic response seen in the numeric spectrogram. Figure 10 is a higher-resolution version of another experimental installation, indicating the strong and weak harmonic regime at a flow speed of approximately $U = 0.41$ with more clarity. Also observable in figure 10 is the broadband response near $U = 0.54$. Although only a single sweep (with increasing flow rate) is shown

in figure 10, this installation also showed a slightly greater range of hysteresis than figure 9. Finally, we note the interesting appearance of transient frequency content prior to the first onset of LCO, i.e. below $U \cong 0.2$. This gradual increase in dynamic activity suggests the possibility of developing a useful diagnostic capability.

Of course, all of the differences presented in the above discussion should be interpreted in the context of nonlinear systems where the possibility of multiple solutions emphasizes the importance of initial condition dependence of solutions.

4. Stability of LCOs

In this section a method for experimentally determining the stability of LCOs is proposed. Results are presented and compared with simulation. The limit cycle chosen for this study was the LCO that exists from approximately $U = 0.45$–1.0 (see figures 3 and 9). The upper flow speed bound seen in numerical simulation was not experimentally verified due to the potential destructive consequence of divergent flutter. This LCO was chosen due to the wide parameter regime over which it exists and due to its clearly distinguishable features (and relatively clean signal). The first experimental method uses a perturbation approach to generate a linearized map (based on a least-squares fit). A subspace scheme using a stochastic input, where the natural turbulence in the wind tunnel provides the disturbance input, was also investigated, but is not reported here. The other experimental approach is intended to give a more qualitative geometric understanding of the system's stability by investigating the basins of attraction of the LCO and a coexisting response as a function of the flow speed. This method also makes use of the gust generator, but with the induced transients being relatively large. Before describing these experimental methods, the basis for the linearized map model is developed using analysis methods from nonlinear dynamics.

(a) Description of linearized map

A fundamental assumption underlying the disturbance approach is that for some neighbourhood about the LCO, perturbations grow or decay exponentially in time. Of course, one could construct examples where this assumption fails for all but the most infinitesimal regions. For example, if the linearization point was *near* a grazing bifurcation often encountered in impacting systems (Begley 1996; Casasa *et al.* 1996), the linearization region could be prohibitively small. In the present case, the flap's sudden encounter with stiffness upon leaving the deadband would act as an impact. This type of behaviour is encountered in the non-periodic regime that coexists with the LCO considered in these stability measurements. This fact indicates the results should be interpreted with some caution.

In order to construct a linear map, a point must be chosen about which the nonlinear system can be linearized. In the absence of a distinct forcing period, and considering the geometric nature of a phase-space representation of the system dynamics (see Strogatz (1994) and Virgin (2000) for examples), a natural choice is the transverse intersection of a prescribed plane in phase space. Figure 11 is a schematic representation of such an intersection, which is known as a Poincaré section. We can thus examine the stability properties of an LCO by its penetration of the system surface of section. This, of course, turns the continuous (differential) flow into a discrete map (with a corresponding reduction of system order of one).
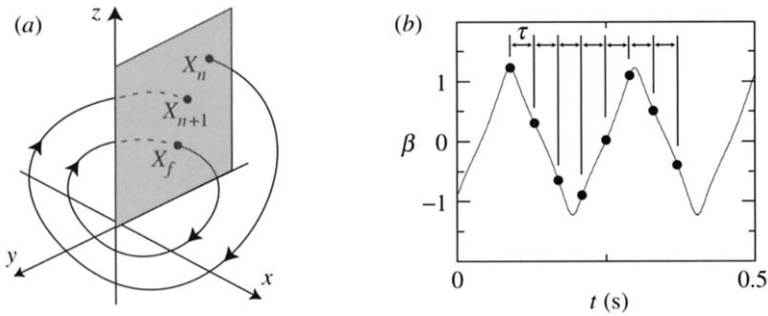
Figure 11. (*a*) Poincaré section schematic. (*b*) Time-delay schematic.

Another concept important for the present work invokes methods for reconstructing system dynamics using only a limited subset of system outputs. Control theorists who typically concern themselves with linearized models of processes have developed an extensive theory of state estimation, with an accompanying set of rigorous requirements necessary to achieve an accurate estimate, namely observability. On a heuristic level, the concept of observability (which can be expressed in terms of the rank of a particular observability matrix) is simply whether all the states of the system can be *seen* in the linear algebra sense of projecting all of the system dynamical states onto the given output space.

Based upon ideas first presented in Packard *et al.* (1980), if only position outputs of the system were accessible, the dynamics of the complete system can be reconstructed or observed using a finite-difference approach to calculate the rates of change of the position. A conceptually related approach, known as the method of time delays (Takens 1981), involves temporally embedding an output within itself (e.g. figure 11). It is easy to see that as the embedding time delay approaches zero, this quantity is related to the calculus time derivative, i.e. velocity. An excellent discussion of the ambiguities inherent in the application of the method of delays to experimental systems, namely the length of the delay and the embedding dimension or number of points to embed, can be found in Broomhead & King (1986). In the present work, an implementation of the method of delays was used to formulate the Poincaré section. This approach was taken due to the signal-to-noise properties of the transducers, with the flap transducer giving the cleanest most-sensitive signal.

When the dimension of the space visited by a dynamic system is known *a priori*, an embedding dimension equal to twice the dimension of the system plus one $(2N + 1)$ is sufficient. In practice, the dimension of the system is usually only approximately known, thus a trial-and-error method of false nearest-neighbours calculations, in which the dimension is systematically increased until trajectories no longer appear to intersect, is often employed (Abarbanel 1996).

Unfortunately, this method becomes less feasible in the presence of noise and as the system dimension increases. Broomhead & King (1986) proposed a method based on developments from information theory, wherein a basis can be determined from the experimentally measured data using singular value decomposition such that reconstructed dynamics remain geometrically invariant upon surpassing a dimensional threshold.

The length of the delay used in the embedding is another ill-defined parameter. The two most widely used conventions are the delay defined by the first zero crossing of the

autocorrelation function for periodic responses and the time specified by the mutual information algorithm for non-periodic responses (Kantz & Schreiber 1999). In the present work, the periodic nature of the LCO suggested the use of the autocorrelation method.

Thus the linearized map about an LCO can be formally defined as

$$(\boldsymbol{X}_{N+1} - \boldsymbol{X}_{\mathrm{f,LCO}}) = A|_{X_{\mathrm{f,LCO}}} \cdot (\boldsymbol{X}_N - \boldsymbol{X}_{\mathrm{f,LCO}}), \qquad (4.1)$$

where A is the map-dynamics matrix, $\boldsymbol{X}_{\mathrm{f,LCO}}$ is the fixed point of the LCO in the Poincaré section and the vectors $\boldsymbol{X}_{N+1}$ and $\boldsymbol{X}_N$ are successive points in the Poincaré section. In this work, the embedded state vector is defined as

$$\boldsymbol{X}_i = [\beta(t_0)\ \beta(t_0 + \tau)\ \cdots\ \beta(t_0 + (n-1)\tau)]^{\mathrm{T}}, \qquad (4.2)$$

where τ is the embedding delay, n is the embedding dimension and t_0 is the time when the flap velocity crosses zero from above ($\dot{\beta} = 0^+$). A typical embedding dimension of 12 and a τ of 0.024 s (corresponding to the first zero crossing of the autocorrelation function at approximately a quarter of an average period of the LCO over the flow range considered) was used in this research.

(b) Least-squares method

The inspiration to attempt a least-squares fit of the dynamics about an LCO came in two forms. The first was the earlier work of Murphy *et al.* (1994), wherein they tracked the stability of two different forced nonlinear oscillators by characterizing the decay of perturbations to the system. The second was an experimental observation of the effectiveness of the gust generator (recall figure 2) at producing perturbations to the system.

In order to estimate the dynamics map matrix A, a series of Poincaré section points $\boldsymbol{X}_N$ and their images $\boldsymbol{X}_{N+1}$ were collected following a perturbation from the gust generator. The gust perturbation was a two-second constant-frequency excitation, where the frequency was selected from a preassigned set of frequencies chosen for their ability to excite the various modes of the system. Figure 12 shows the time history of the flap at a speed of $U = 0.497$, with the gust generator turned on at a time of approximately $t = 0.7$ s. In this case, the gust generator is tuned to the plunge excitation frequency. The generator is then switched off after two seconds and the system decays back to the original stable LCO. As can be seen, the LCO's stability is robust to a large perturbation at this flow condition. Figure 12 shows a typical sequence of points in the Poincaré section at a flow speed of $U = 0.632$ following perturbations from the gust generator. The first five elements of the 12-element vector are plotted against the penetration index, an integer index labelling successive intersections with the surface of section used to define the Poincaré sampling.

The actual least-squares fit was performed using the MATLAB software package, where a pseudo-inverse solution to the least-squares problem was used,

$$A = \boldsymbol{X}_{N+1} \cdot \boldsymbol{X}_N^{\mathrm{T}} (\boldsymbol{X}_N \cdot \boldsymbol{X}_N^{\mathrm{T}})^{-1}. \qquad (4.3)$$

At this point, it should be mentioned that, with the present gust-generator system, the slotted cylinder came to rest at an arbitrary angle after each perturbation. The angle of the cylinder would then lead to an effective angle of attack on the airfoil. The net effect was that each steady-state LCO was a (weak) function of the unknown final resting angle of the slotted cylinder, although this effect was found to be relatively minor.
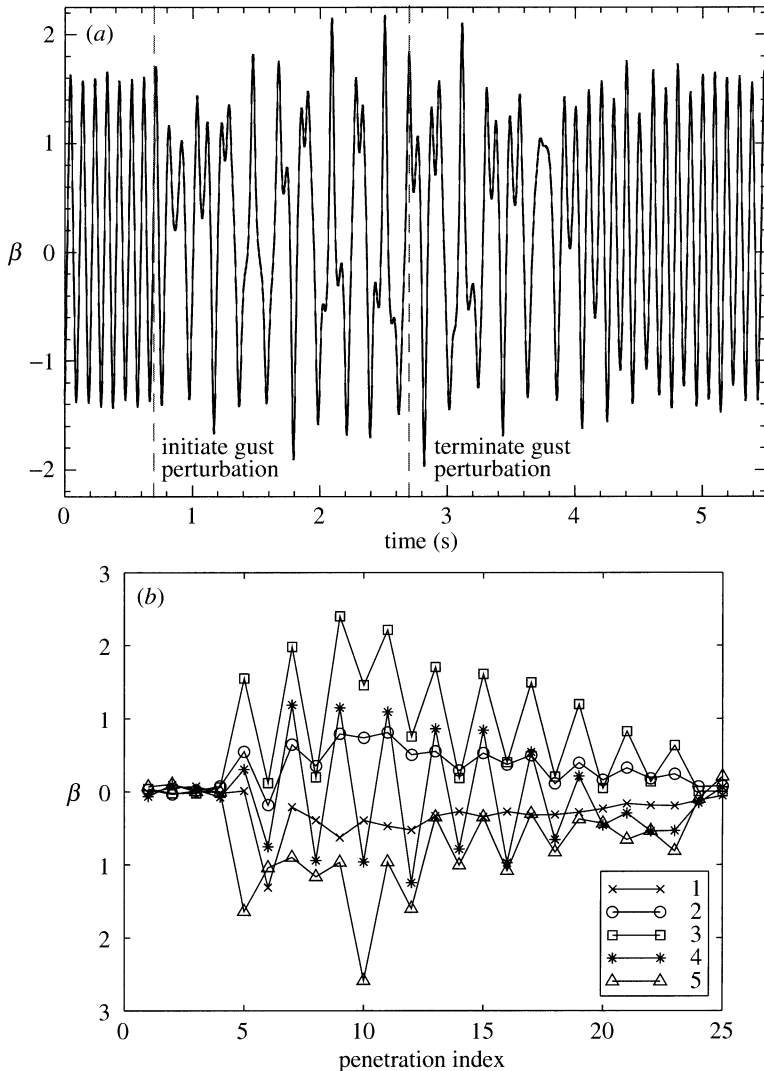
Figure 12. (*a*) Time history of flap motion incorporating a plunge perturbation. (*b*) Perturbation Poincaré history from section index 0 to 25. The vertical axis shows flap angle displacement for the first through fifth point in the embedded Poincaré section. The penetration index does not necessarily correspond to constant time increments.

5. Local stability results

As a frame of reference, results from the least-squares method using experimental data are initially compared with a finite-difference computation of the Jacobian of the Poincaré mapping. The experimental results do not show a close quantitative match to the numerical simulation results. Thus figure 13 should be used as a (numerical simulation) guide to interpreting the experimental results to follow. In figure 13*a*, eigenvalues of the Jacobian matrix travel toward the unit circle as the flow speed decreases. In the case of a (smooth) map, stability is indicated by location of eigenvalues relative to the unit circle. Values inside the circle indicate a stable oscillation,
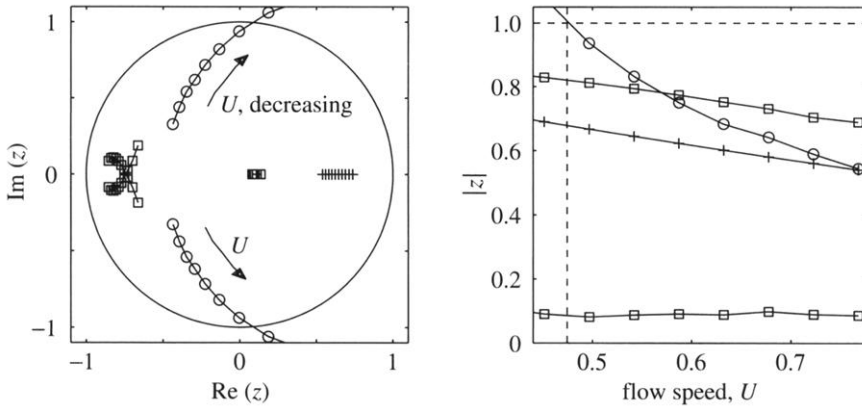
Figure 13. Example finite-difference result.

while values outside the circle indicate an unstable system. The type of bifurcation that occurs after the loss of stability is indicated by the location of the eigenvalue that pierces the unit circle. Eigenvalues crossing the unit circle on the positive real axis indicate a fold or saddle-node bifurcation (Virgin 2000). Eigenvalues crossing the unit circle on the negative real axis indicate a flip or period-doubling bifurcation. Complex conjugate pairs of eigenvalues that pierce the unit circle indicate a Neimark bifurcation. Thus we observe that the magnitude of one of the eigenvalues reaches unity close to $U = 0.47$, which agrees with the (decreasing flow rate) bifurcation diagram in figure 3. The resulting behaviour is aperiodic.

In the experiments performed to measure LCO stability, the problem was typically overconstrained in the sense that the order or dimension of the dynamics map matrix was assumed to be larger than the analytically suggested order of nine (based on the three structural degrees of freedom, their derivatives and the additional effects of the aerodynamics). In the least-squares experiments, the embedding dimension was set at 12. The metric used in determining the number of embeddings was actually based on a threshold in singular value decompositions (Broomhead & King 1986). As a consequence of overconstraining the problem, additional eigenvalues appear that are not physically meaningful. A strategy to reduce these additional eigenvalues was based on the assumption that physically meaningful eigenvalues would remain invariant across different experiments. Thus closely clustered eigenvalues were selected as valid data points, while disparate values were excluded.

The perturbation least-squares experiment was performed on the experimental aeroelastic system corresponding to the spectrogram plot of figure 10. A set of approximately 20 perturbations were used to accumulate 500 Poincaré points X_i and their images X_{i+1} at a given flow speed. An embedding dimension of 12 was used. Following a perturbation, point pairs (X_i, X_{i+1}) were collected until the system returned to within a small region of the fixed point of the LCO. Once the set of data was collected, a least-squares fit was performed to determine a dynamics matrix A. Next, the eigenvalues of A were calculated and recorded. The flow speed was then set at the next flow speed setting and the process was repeated. This set of experiments was run over a range of flow speeds and repeated several times at each flow speed.
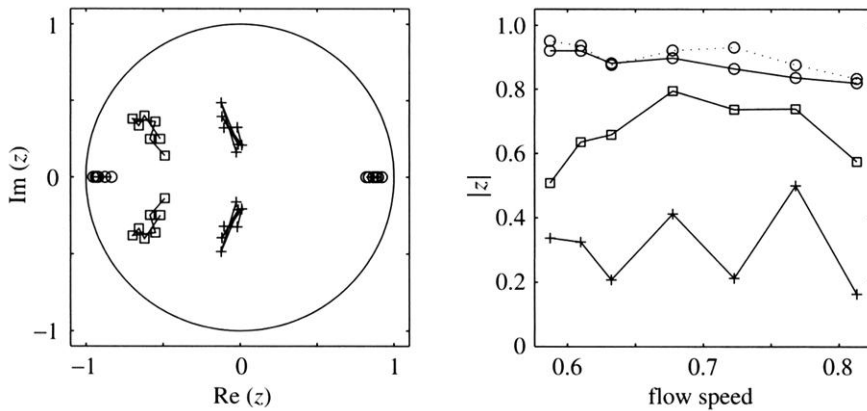
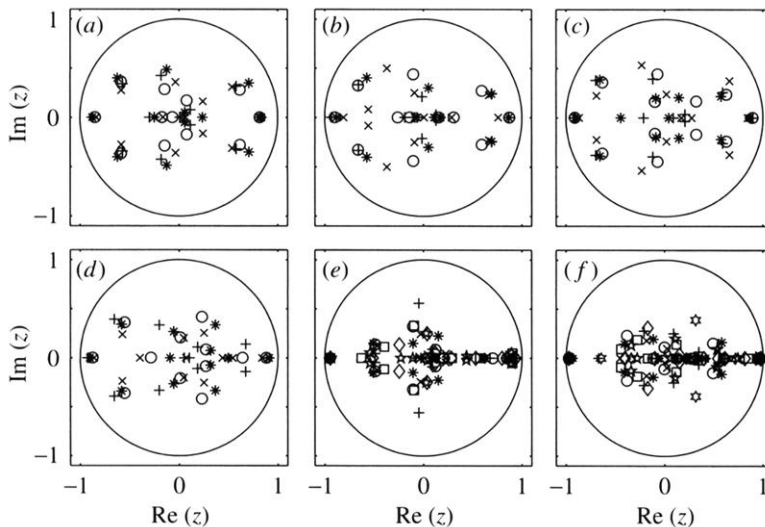Figure 14. Processed eigenvalues of least-squares method (order = 12).

Figure 15. Unprocessed eigenvalues of least-squares method (order = 12). Non-dimensional flow speeds of (a) 0.768, (b) 0.723, (c) 0.678, (d) 0.632, (e) 0.597 and (f) 0.542. Here, the different symbols represent different experimental runs.

In this first experiment, no eigenvector information was recorded, so the eigenvalue invariance assumption was applied to reduce the full dataset seen in figure 15 to the processed form of figure 14. The type of bifurcation indicated by the path taken by the eigenvalue to exit the unit circle is clearly different in figure 14 than in figure 13. In figure 13 the eigenvalues suggest a Neimark bifurcation, while in figure 14 the eigenvalues on the real axis are heading toward the unit circle, indicating either a flip- or a fold-type bifurcation. The approach of the loss of instability for the LCO appears to be consistent with the results of the spectrogram in figure 10, where the LCO at high flow speeds gives way to a different type of response near $U = 0.58$, although only the increasing flow rate case is shown. Clearly, there is a bifurcation, but due to the noise in the system, the post-transition behaviour is not easy to categorize. The raw data of figure 15 indicate the degree of variability seen in the calculated eigenvalues at different flow speeds.
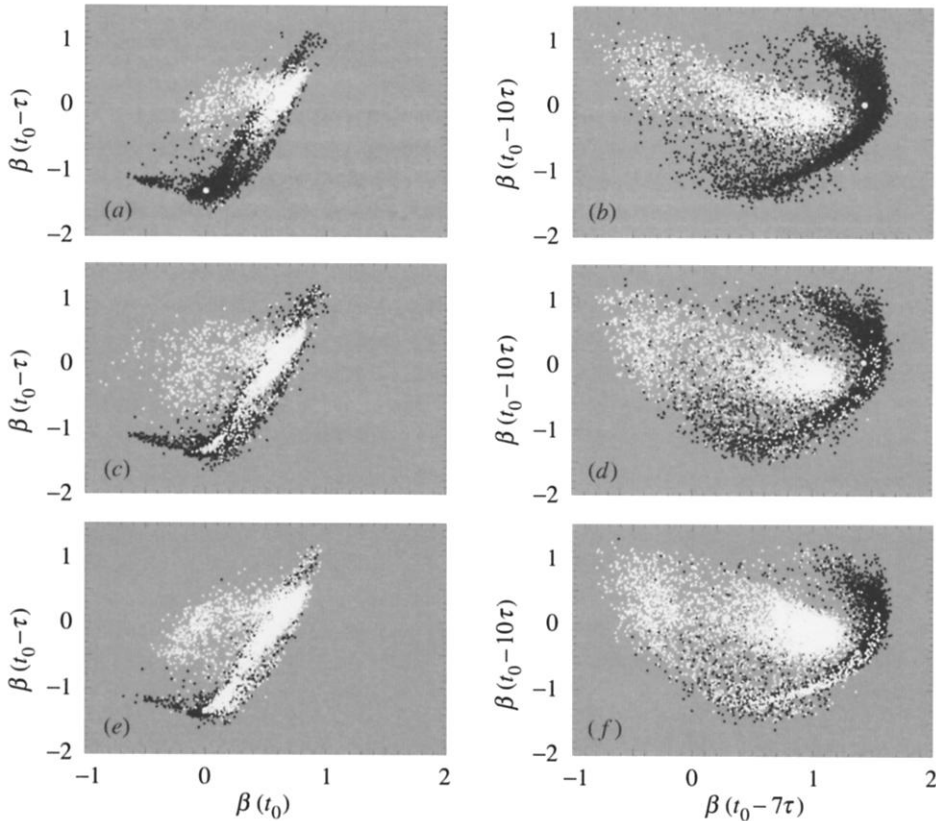
Figure 16. Basins of attraction (experimental). (*a*), (*b*) $U = 0.452$. (*c*), (*d*) $U = 0.438$. (*e*), (*f*) $U = 0.431$. White data points correspond to a low-frequency response, black to a high-frequency (buzz) response.

6. Basins of attraction

An additional measure of system stability that is global, rather than local, in nature is the basin of attraction for a given response. From the perspective of linear systems, basins are either all space or zero space, as there are no coexisting solutions for linear systems. For nonlinear systems, there are often multiple, or competing, responses. The long-term steady-state solution typically depends on the initial conditions of the problem.

For the experimental aeroelastic system, a set of initial conditions were produced using relatively large perturbations via the slotted cylinder gust generator. The problem of the post-perturbation arbitrary cylinder angle remained. However, the results indicate a qualitative indicator of the change in basin size despite experimental variability.

Figure 16 tracks the evolution of the basins of attraction for the LCO response studied in the stability tests above, i.e. a flap 'buzzing' response (labelled high frequency), as well as a lower-frequency non-periodic tapping-type response (labelled low frequency). The generated initial conditions (in this projection) that lead to either of the two attractors are thus shaded according to the scheme given in the

Table 2. *Basin of attraction data showing the relative dominance of the two attractors in the hysteresis region of the experimental system*

flow speed U (m s^{-1})	unknown basin number (%)	low-frequency basin number (%)	high-frequency basin number (%)
0.452	1100 (11.0)	1850 (18.5)	7050 (70.5)
0.438	600 (6.0)	3300 (33.0)	6100 (61.0)
0.431	50 (0.5)	6350 (63.5)	3600 (36.0)

figure caption. These LCOs coexist in the region of hysteresis that lies approximately over the narrow flow range $U = 0.452$–0.431 (see figure 10). As experimental measurements progressed, methods for identifying the distinct response improved. Thus, for the earlier cases (higher flow speed), the number of points that could not be successfully identified as belonging to either the high- or low-frequency basin is significantly larger.

Figure 16 indicates, in a geometric sense, that the high-frequency LCO is losing its stability, or robustness to withstand disturbance, as the flow velocity decreases. Two different projections are shown, using delays of τ and 3τ. Table 2 details the number out of 10 000 initial conditions that were attracted to each basin. The general trend is clear, i.e. that the high-frequency response is attracting a smaller share of the total initial conditions and hence is losing dominance as the flow rate is decreased (again, the global loss of stability occurs at about $U = 0.43$).

Given the relatively high dimension of the system, it is clear that establishing comprehensive details about the domains of attraction is a daunting task, and hence the projections shown represent an initial step in acquiring global stability information from a realistic aeroelastic system. We also note that the table of initial conditions is particularly useful when one considers that the basin plots in figure 16 are clearly affected by the order in which the data-point shades are plotted, e.g. many black data points are obscured by the white data points in figure 16f.

Finally, an analogous study of some basins of attraction is conducted for numerical simulation of the equations of motion. Since a thorough investigation of initial conditions is intractable for this moderately complex system, the approach adopted here consists of randomly generating a representative set of initial conditions, not dissimilar to the method used in the experimental perturbation approach above, i.e. a located fixed point is subject to a variety of disturbances. The subsequent destination of a trajectory at an instant of time (a surface of section), consistently defined after each disturbance, is tracked and assigned to an attractor.

Figure 17 shows coexisting solutions at three (increasing) values of the flow rate. Rather than superimposing the attractors on the same diagram, they are separated for clarity. The control-parameter values at which these snapshots were taken are slightly different from the experimental values and, indeed, one of the coexisting attractors in this region of hysteresis is aperiodic (and hence no fixed point is defined). The banded nature of the aperiodic attractor is suggestive of quasi-periodicity and a transition to chaos—a feature observed in simulations of a similar system (Virgin *et al.* 1999). Here, only a single delay of 3τ is used in the reconstruction, since the projection in this plane was relatively well defined.
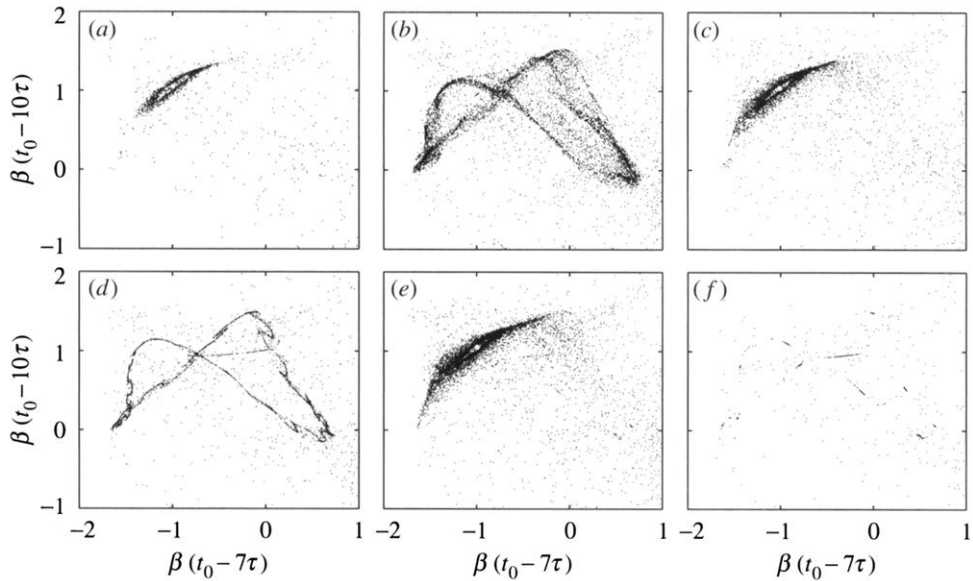
Figure 17. Basins of attraction (numerical). (a), (b) $U = 0.478$. (c), (d) $U = 0.485$. (e), (f) $U = 0.492$. Parts (a), (c) and (e) correspond to a simple periodic attractor, while parts (b), (d) and (f) correspond to an aperiodic response.

7. Conclusions

This paper presents some detailed experimental and theoretical evidence of LCOs in a three-degree-of-freedom airfoil system with a freeplay in the flap. These types of 'buzz' response have been observed in a number of practical situations and have obvious implications for aircraft safety and maintenance scheduling. Relatively new techniques (from largely numerical developments) in nonlinear dynamical systems theory provide a useful framework for characterizing the behaviour of this type of motion. The stability of LCOs is viewed from both a local and global perspective and the results presented in this paper indicate the utility of methods of nonlinear dynamics in the context of wind-tunnel experiments. The results presented here also point toward developing techniques for the online monitoring of dynamic behaviour with a view to predicting (undesirable) responses as a parameter approaches a bifurcation condition.

References

Abarbanel, H. D. I. 1996 *Analysis of observed chaotic data.* Springer.

Alighanbari, H. & Price, S. J. 1996 The post-Hopf-bifurcation response of an airfoil in incompressible two-dimensional flow. *Nonlin. Dynam.* **10**, 381–400.

Begley, C. J. 1996 The nonlinear dynamics of an impact oscillator with friction: theory and experiment. PhD thesis, Duke University.

Breitbach, E. J. 1977 Effect of structural nonlinearities on an aircraft vibration and flutter. Technical Report 665, AGARD.

Broomhead, D. S. & King, G. P. 1986 Extracting qualitative dynamics from experimental data. *Physica* D **20**, 217–236.

Casasa, F., Chin, W. F., Grebogi, C. & Ott, E. 1996 Universal grazing bifurcations in impact oscillators. *Phys. Rev.* E **53**, 134–139.

Cizmas, P. G. A., Tang, D. & Dowell, E. H. 1996 Flow about a slotted cylinder-airfoil combination in a wind tunnel. *J. Aircraft* **33**, 716–721.

Conner, M. D. 1996 Nonlinear aeroelasticity of an airfoil section with control surface freeplay. PhD thesis, Duke University.

Conner, M. D., Tang, D. M., Dowell, E. H. & Virgin, L. N. 1997 Nonlinear behavior of a typical airfoil section with control surface freeplay: a numerical and experimental study. *J. Fluids Struct.* **11**, 89–109.

Dowell, E. H., Crawley, E. F., Curtiss, H. C., Peters, D. A., Scanlan, R. H. & Sisto, F. 1995 *A modern course in aeroelasticity.* Dordrecht: Kluwer Academic.

Edwards, J. W., Ashley, H. & Breakwell, J. V. 1979 Unsteady aerodynamic modeling for arbitrary motions. *AIAA J.* **17**, 365–374.

Henon, M. 1982 On the numerical computation of Poincaré maps. *Physica* D **5**, 412–414.

Kantz, H. & Schreiber, T. 1999 *Nonlinear time-series analysis.* Cambridge University Press.

Lee, B. H. K. & Tron, A. 1989 Effects of structural nonlinearities on flutter characteristics of the CF-18 aircraft. *J. Aircraft* **26**, 781–786.

Lee, B. H. K., Gong, L. & Wong, Y. S. 1997 Analysis and computation of nonlinear dynamic response of a two-degree-of-freedom system and its application in aeroelasticity. *J. Fluids Struct.* **11**, 225–246.

Lee, B. H. K., Price, S. J. & Wong, Y. S. 1999*a* Nonlinear aeroelastic analysis of airfoils: bifurcation and chaos. *Prog. Aerosp. Sci.* **35**, 205–334.

Lee, B. H. K., Jiang, L. Y. & Wong, Y. S. 1999*b* Flutter of an airfoil with a cubic restoring force. *J. Fluids Struct.* **13**, 75–101.

McIntosh, S. C., Reed, R. E. & Rodden, W. P. 1981 Experimental and theoretical study of nonlinear flutter. *J. Aircraft* **18**, 1057–1063.

Murphy, K. D., Bayly, P. V., Virgin, L. N. & Gottwald, J. A. 1994 Measuring the stability of periodic attractors using perturbation-induced transients: applications to two nonlinear oscillators. *J. Sound Vib.* **172**, 85–102.

O'Neil, T. & Stragnac, T. W. 1998 Aeroelastic response of a rigid wing supported by nonlinear springs. *J. Aircraft* **35**, 616–622.

Ott, E. 1993 *Chaos in dynamical systems.* Cambridge University Press.

Packard, N. H., Crutchfield, J. P., Framer, J. D. & Shaw, R. S. 1980 Geometry from a time series. *Phys. Rev. Lett.* **45**, 616–622.

Peters, D. A. & Cao, W. 1995 Finite state induced flow models part I. Two-dimensional thin airfoil. *J. Aircraft* **32**, 313–322.

Press, W. H., Teukolsky, S. A., Vetterling, W. T. & Flannery, B. P. 1992 *Numerical recipes in C: the art of scientific computing.* Cambridge University Press.

Price, S. J., Lee, B. H. K. & Alighanbari, H. 1994 Post-instability behavior of a 2-dimensional airfoil with a structural nonlinearity. *J. Aircraft* **31**, 1395–1401.

Price, S. J., Alighanbari, H. & Lee, B. H. K. 1995 The aeroelastic response of a 2-dimensional airfoil with bilinear and cubic structural nonlinearities. *J. Fluids Struct.* **9**, 175–193.

Raghothama, A. & Narayanan, S. 1999 Non-linear dynamics of a two-dimensional airfoil by incremental harmonic balance method. *J. Sound Vib.* **226**, 493–517.

Shen, S. F. & Hsu, C. C. 1958 Analytical results of certain nonlinear flutter problems. *J. Aeronaut. Sci.* **25**, 136–137.

Strogatz, S. H. 1994 *Nonlinear dynamics and chaos.* Addison-Wesley.

Takens, F. 1981 Detecting strange attractors in turbulence. In *Dynamical systems and turbulence* (ed. D. A. Rand & L.-S. Young). Springer Lecture Notes in Mathematics, vol. 898, pp. 366–81. Springer.

Tang, D. M. & Dowell, E. H. 1996 Nonlinear response of a non-rotating rotor blade to a periodic gust. *J. Fluids Struct.* **10**, 721–742.

Tang, D. M., Cizmas, P. G. A. & Dowell, E. H. 1996 Experiments and analysis for a gust generator in a wind tunnel. *J. Aircraft* **33**, 139–148.

Tang, D. M., Dowell, E. H. & Virgin, L. N. 1998 Limit cycle behavior of an airfoil with a control surface. *J. Fluids Struct.* **12**, 839–858.

Trickey, S. T. 2000 Global and local dynamics of an aeroelastic system with a control surface freeplay nonlinearity. PhD thesis, Duke University.

Virgin, L. N. 2000 *Introduction to experimental nonlinear dynamics.* Cambridge University Press.

Virgin, L. N., Dowell, E. H. & Conner, M. D. 1999 On the evolution of deterministic non-periodic behavior of an airfoil. *Int. J. Nonlin. Mech.* **34**, 499–514.

Woolston, D. S., Runyan, H. L. & Byrdsong, T. A. 1955 Some effects of system nonlinearities in the problem of aircraft flutter. Technical Report 3539, NACA.

Woolston, D. S., Runyan, H. L. & Andrews, R. E. 1957 An investigation of effects of certain types of structural nonlinearities on wing and control surface flutter. *J. Aeronaut. Sci.* **24**, 57–63.

Yang, Z. C. & Zhao, L. C. 1992 Transition of the flutter mode of a 2-dimensional section with an external store. *J. Aircraft* **29**, 511–512.